Sustainable Marine Structures
https://journals.nasspublishing.com/sms

ARTICLE

Model Setup Evaluation for Two-Dimensional Physical Model of Wave-Structure Interaction for Modular Floating Photovoltaic

Maria Angelin Naiborhu [1*] , ***Ricky Lukman Tawekal*** [2] , ***Ahmad Muchlis Firdaus*** [2] , ***Farid Putra Bakti*** [2] , ***Eko Charnius Ilman*** [2] , ***Reynard Alexander Zebua*** [2] , ***Hasya Farhana*** [2] , ***Jesa Angelin*** [2] , ***Alfiza Aulia*** [2] , ***Adinda Putri Kania Hermanto*** [2] , ***Nathaniel Leonard Setiono*** [2] , ***Muhamad Rayhan Khashib*** [2] , ***Ahmad Safii Maarif*** [2]

[1] *Department of Civil Engineering, Faculty of Civil and Environmental Engineering, Institut Teknologi Bandung, Bandung 40132, Indonesia*

[2] *Department of Ocean Engineering, Faculty of Civil and Environmental Engineering, Institut Teknologi Bandung, Bandung 40132, Indonesia*

ABSTRACT

Interest in understanding the structural behavior of marine floating photovoltaic (FPV) systems has grown significantly over the last decade. Numerical models are the preferred approach for understanding FPV responses under environmental loads, but they require validation. Several methods are commonly used to validate numerical results, such as comparison with analytical, field data, and experimental data. The use of analytical approaches to validate numerical results can sometimes be inaccurate due to the complexity of the problems; nevertheless, field data is commonly restricted and frequently unavailable for numerical model validation. Thus, physical models play a crucial role in validating numerical results. This study focuses on the two-dimensional (2-D) modeling process and sensors development for an FPV system with taut mooring, aiming to investigate wave-structure interaction while considering hydroelastic effects. The model is developed in accordance with the

*CORRESPONDING AUTHOR:
Maria Angelin Naiborhu, Department of Civil Engineering, Faculty of Civil and Environmental Engineering, Institut Teknologi Bandung, Bandung 40132, Indonesia; Email: 35022003@mahasiswa.itb.ac.id

ARTICLE INFO
Received: 10 September 2025 | Revised: 15 October 2025 | Accepted: 24 October 2025 | Published Online: 2 December 2025
DOI: https://doi.org/10.36956/sms.v7i4.2719

CITATION
Naiborhu, M.A., Tawekal, R.L., Firdaus, A.M., et al., 2025. Model Setup Evaluation for Two-Dimensional Physical Model of Wave-Structure Interaction for Modular Floating Photovoltaic. Sustainable Marine Structures. 7(4): 132–149. DOI: https://doi.org/10.36956/sms.v7i4.2719

Froude-Cauchy similitude law and is made from composite materials to capture structural stiffness. Structural motions, specifically heave and pitch, are measured using an Inertial Measurement Unit (IMU), while strain gauges measure structural stress and mooring tension. The sensors provide precise measurements for strain and pitch; however, heave, as a result of time-domain integration from acceleration, requires further validation. The motion responses of the model align with reference results.

Keywords: Composite Model; 2-D Experimental; Floating Photovoltaic; Froude-Cauchy Similitude; Hydroelastic

1. Introduction

Interest in floating photovoltaic (FPV) deployment in both offshore and nearshore marine environments has grown significantly over the past decade, providing renewable-based power in many countries [1,2]. Comprehensive review of FPV development in the marine environment has been presented in numerous publications [3–6]. The nearshore FPV installation with a capacity of 5.0 Mega Watt-peak (MWp) in the Strait of Johor-Singapore sets the stage for more potential development of marine FPV in the nearshore region [7]. This region is favored due to its relatively less harsh than the offshore environment, where recent advancements in onshore FPV technology may still be applicable [6].

Recent developments in FPV structures have largely adopted a modular configuration. In this design, individual floater units serve as buoyant platforms that support photovoltaic (PV) panels and provide operational access for maintenance activities. These modules are typically fabricated from high-density polyethylene (HDPE), a material selected for its durability, buoyancy, and resistance to environmental degradation. Structural assembly is achieved through pin-jointed connections, enabling for the creation of a large floating platform. To maintain position, mooring systems are integrated into the structure, counteracting environmental forces and restricting excessive displacement. The modularity of the FPV structures requires connectors to connect individual floater modules, which restrict the six degrees of freedom (6-DOF) motions of the connected floater modules. Based on the type of primary restricted motion, the connector can be classified into rigid and flexible connectors [8,9]. The key distinction between these types lies in the transmitted of bending moments, with rigid connectors being the commonly used in recent FPV structure.

A typical FPV installation with a capacity of 1 MWp extends over several hundred meters in width and length while maintaining a relatively low freeboard, often below 0.5 m. The pronounced disparity between its lateral dimensions and vertical extent results in a highly flexible structure, wherein hydroelastic behavior plays a dominant role in its response to external forcing. Consequently, the dynamic interaction between hydrodynamic loads and structural deformation must be carefully considered in its analysis.

Extensive numerical and experimental investigations have been conducted to characterize the response of FPV systems under environmental loads, particularly wave, wind, and current forcing. A range of analytical and computational approaches have been employed to predict the hydroelastic response of large, flexible floating structures, including methodologies specifically adapted for FPV platforms. Key contributions to this domain are presented in the literature, including works by Fu et al. (2007)[10], Kim et al. (2025)[11], Liu and Sakai (2002)[12], Li et al. (2023)[13], Jiang et al. (2024)[14], Shi et al. (2023)[15], Xu and Wellens (2022)[16], Zhang and Schreier (2022)[17], which provide a foundation for further refinement of predictive models and structural optimization strategies.

During the early development stage of an FPV system with a certain design, it is important to do hydrodynamic analysis to study the interaction between disturbing forces and the floating structure. However, as the FPV systems are subject to various environmental loads, dominantly waves and winds, and the structural responses are highly non-linear which may not be fully represented in numerical models, then experimental modelling holds a critical role to validate the numerical results.

To validate numerical results, an experimental study with a certain model scale is required, as full-

scale experiments on large floating structures are generally not possible. The scaling of FPV as a large floating structure will be challenging due to several issues: (i) the dimension of the floating structure, (ii) the scaling of bending stiffness, and (iii) the structure's modularity [4]. Structural bending stiffness plays an important role in hydroelastic response, but satisfying the similarity of bending stiffness in a large floating structure is very difficult as the mass scale shall be maintained as well. A review of the modeling approach and scaling strategies for marine floating structure is discussed in Chakrabarti (1998)[18], Ruzzo et al. (2021)[19], Vassalos (1998) [20], Bakti et al. (2021) [21], Jin et al. (2025)[22], Loe et al. (2025)[23].

This paper aims to provide information on two-dimensional (2-D) physical modeling and scaling strategies for modular FPV with a mooring system in nearshore area. Similitude, scaling law, dimensional analysis and model development to capture hydroelastic response are described, along with the experimental setup. As the experiment requires various types of sensors in large numbers, low-cost customized sensors are made. The performance of these self-developed and low-cost customized sensors is also discussed along with the model performance. To simulate the hydroelastic effect to the structure in 2-D, the model is made of composite materials, a similar method to those used in large ship hydrodynamic models [24]. The detail for experimental results will be discussed in a separate paper.

2. Dimensional Analysis and Modeling Scheme

Dimensional analysis is a method used to combine physical variables into a set of dimensionless products, thereby reducing the number of variables that need to be considered [25]. To define the variables for this experiment, it is important to define the purposes of the experiment. As the main purpose of this experiment is to study the dynamic response, specifically the pitch and heave motion, of a modular FPV system under wave loads, then the physical variables to be included are: wave and fluid properties, characteristics of the FPV and its mooring line, and the structural response.

The hydrodynamics variables include wave height (H), wave length (L), wave period (T), water depth (h), water density (ρ_w); while the fluid properties are: fluid dynamic viscosity (μ), local flow velocity (υ), and gravity acceleration (g). The variables representing the FPV structure and mooring line are: width (B_f), length (L_f), height (D_f), total weight of floaters (m_f) and flexural rigidity (EI) of the structure; and elastic stiffness (k_m) for mooring line. The structural responses are represented by pitch (R_y) and heave (Z_h). Based on those variables, the FPV response is written as a function (f) of:

$$f(H, L, T, h, \rho_w, \mu, \upsilon, g, B_f, L_f, D_f, m_f, \mathrm{EI}, k_m, R_y, Z_h) = 0 \qquad (1)$$

By following Buckingham Pi Theorem methodology, there are many possible combinations of non-dimensional products that can be obtained, however the most relevant for this experiment are:

$$F = \left(\frac{H}{L}, \frac{H}{gT^2}, \frac{h}{gT^2}, \frac{h}{L}, \frac{v}{\sqrt{gL_f}}, \frac{L_f \rho_w v}{\mu}, \frac{\rho_w v^2}{E}, \frac{Z_h}{H}, \frac{L}{L_f}, \frac{m_f g L_f B_f}{EI}, R_y \right) \qquad (2)$$

The first four dimensionless parameters are related to the wave condition, while the fifth parameter is the Froude number, followed by Reynold and Cauchy number. The last four parameters are related to structural responses, in which R_y is considered as a dependent variable. Eq. (2) implies that the set of dimensionless parameters remains the same between the model and the prototype for a particular set of wave conditions. However, since this experiment involves free-surface, gravity-dominated flow, the Reynolds number is not considered because viscous effects are assumed to be negligible.

3. Model Development

3.1. Similitude and Scaling

A requisite for a complete similarity is that the model be geometrically, kinematically and dynamically similar to the prototype. Geometric similarity implies

that the ratio of length $(L)_\Upsilon$ between prototype $(L)_\mathrm{p}$ and model $(L)_\mathrm{m}$ is equal and written as:

$$\frac{L_p}{L_m} = L_\Upsilon \tag{3}$$

where the subscripts m and p are representing model and prototype respectively, while Υ denotes the scale ratio.

Kinematic similarity requires the ratio of prototype velocities to model velocities to be the same. For free-surface flow, kinematic similitude is satisfied when the ratio of the Froude number between the prototype and model is equal as:

$$\frac{V_m}{(g_m L_m)^{\frac{1}{2}}} = \frac{V_p}{(g_p L_p)^{\frac{1}{2}}} \tag{4}$$

Since gravity acceleration (g) cannot be scaled, then $g_\mathrm{m} = g_\mathrm{p}$, hence Eq. (4) can be written as:

$$\frac{V_m}{(L_m)^{\frac{1}{2}}} = \frac{V_p}{(L_p)^{\frac{1}{2}}} \tag{5}$$

The velocity and time ratio are obtained as:

$$V_\Upsilon = L_\Upsilon^{\frac{1}{2}} \tag{6}$$

$$T_\Upsilon = L_\Upsilon^{\frac{1}{2}} \tag{7}$$

Dynamic similarity ensures equality in prototype force to model. It requires that the Froude number of the prototype and model be equal to achieve similar wave behavior under gravity-driven forces. In addition, Froude similitude must satisfy Cauchy similitude as hydroelasticity is considered in the experiment, and can be expressed as:

$$\frac{\mathrm{EI}_p}{\mathrm{EI}_m} = \Upsilon^5 \tag{8}$$

where *EI* is the structural rigidity. In this experiment, the value for *EI* for the connection between floaters is based on Dai et al. (2020) [26]. Given that the model in this experiment used two connectors for one side of the floater, the *EI* assigned to each connector is considered to be half of the total value.

The scale ratio between the prototype and model is 1:10. This ratio is taken by considering the size and capacity of the wave flume, measurement accuracy, and material availability. By applying Froude-Cauchy similitude, the scale factors for the main variables involved in this experiment have been derived and summarized in **Table 1**.

Table 1. The scale factor for the main variables in an NFPV physical model based on Froude-Cauchy's similitude.

Parameter	Unit	Prototype	Model
Hydrodynamic			
Wave period (T)			
· wave period (T), for regular wave	s	4.7; 6.3; 7.9; 9.5	1.5; 2.0; 2.5; 3.0
· Peak wave period (T_p), for irregular wave	s	4.1; 7.3	1.3; 2.3
Wave height (H)			
· wave height (H), for regular wave	m	1.0; 1.5; 2.0	0.1; 0.15; 0.2
· Significant wave height (H_s), for irregular wave	m	1.0; 2.0	0.1; 0.2
Water depth (h), at the wave generator	m	8.0; 6.0	0.8; 0.6
Floater characteristics			
Total length (L_f)	m	25.44	2.544
Total width (B_f)	m	11.4	1.14
Height (D_f)	m	0.2	0.02
Total weight of floaters (m_β), not included PV panels and electrical components	kg	962.63	0.962
Weight of individual PV panel and its electrical components (attached to each of PV floater)	kg	32.2	0.0322
Flexural rigidity (EI)	Nm^2	519.75	0.00520
Mooring Line characteristic			
Axial stiffness (EA)	kN	13.6×10^3	13.6

3.2. Modular FPV Model Development

The modular FPV structure typically consists of several types of floaters units with varying geometries, interconnected by vertical pin connectors. A PV floater unit is designed to have a PV panel mounted on it and is linked to another PV floater in a row. Both ends of the PV floaters row are connected to side floaters, forming a complete floating module. The side floaters also function as platform for access walkways and electrical components.

The modular FPV model development in this experiment is based on a prototype licensed by Flot-Indonesia. This experiment scales down a small section of a large FPV island with a capacity of 1.0 MWp. The prototype of the island has a size of 144.2 m (length) × 47.0 m (width) × 0.2 m (height). The model represents only a small section of the prototype, with dimensions of 24.44 m (length) × 11.44 m (width) × 0.2 m (height), and comprises 64 PV floaters and 77 side floaters, as shown in **Figure 1**. The side floaters have three different sizes, as defined in **Table 2**.

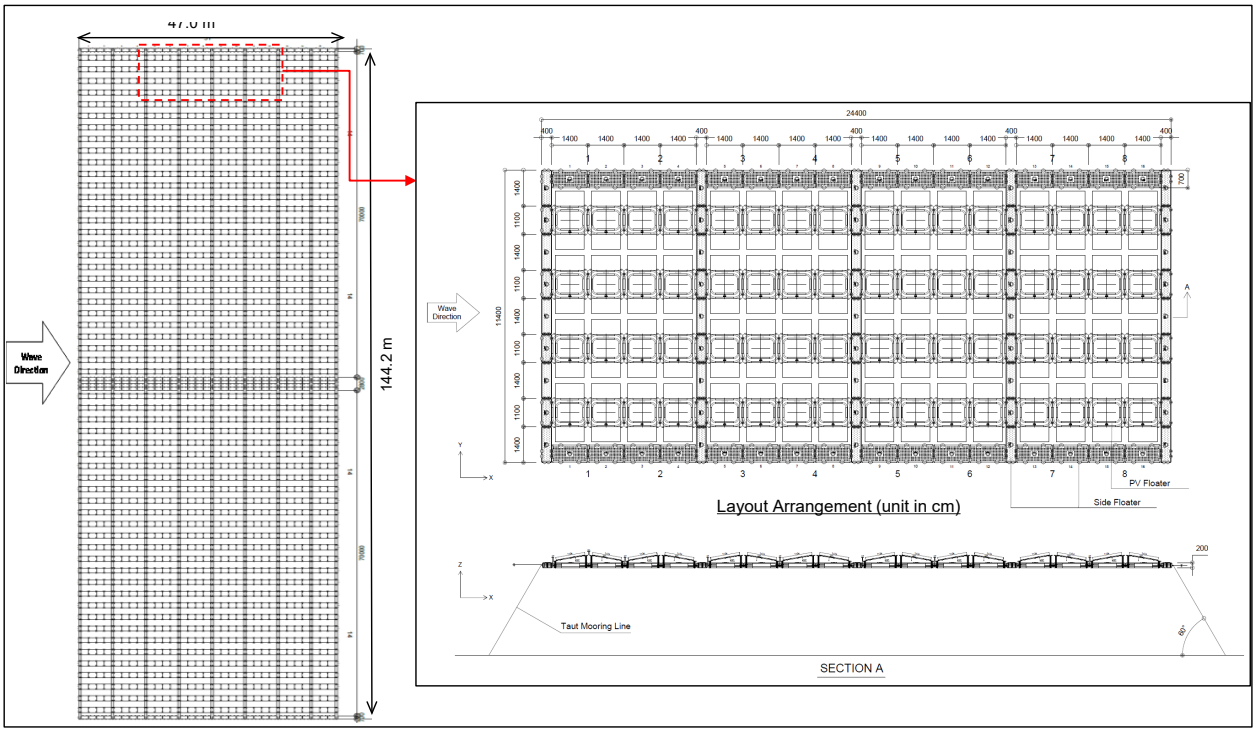

Figure 1. Layout and section arrangement for the prototype of a modular FPV structure.

Table 2. Summary of scaling results for model components.

Parameter	Unit	Prototype	Target Model	Achieved Value
Dimension of Floater Model (length × width × height)				
PV Floater	m	1.4 × 1.1 × 0.2	0.14 × 0.11 × 0.002	
Side Floater Type 1	m	1.4 × 0.7 × 0.2	0.14 × 0.07 × 0.002	
Side Floater Type 2	m	1.4 × 0.4 × 0.2	0.14 × 0.04 × 0.002	
Side Floater Type 3	m	1.1 × 0.4 × 0.2	0.11 × 0.04 × 0.002	
Individual weight of Floater Model				
PV Floater	kg	7.32 (39.52)[1]	0.00732 (0.03952)[1]	0.00598
Side Floater Type 1	kg	8.50	0.0085	0.00783
Side Floater Type 2	kg	6.29	0.00629	0.004
Side Floater Type 3	kg	4.99	0.00499	0.00314

Table 2. *Cont.*

Parameter	Unit	Prototype	Target Model	Achieved Value
Individual weight of Connector Beam				
Connector Beam A	gr	-	5.78 (7.27)[2]	
Connector Beam B	gr	-	0.33 (1.25)[2]	
Connector Beam C	gr	-	1.40	
Horizontal pin connector	gr	-	1.45	
Individual weight of Sensor				
IMU	gr	-	5.79	
SG with a half Wheatstone bridge	gr		1.49	
SG with a quarter Wheatstone bridge	gr		0.92	
Mooring Line characteristic				
Axial stiffness (*EA*)	kN	13.6×10^3	13.6	1.36
Mechanical Property of Floater Model				
Flexural rigidity (*EI*)	Nm^2	519.75	0.0052 (0.0026 for each connector)	

Note: [1] the value in parentheses indicates the weight of the PV floater including PV panels and accessories; [2] the value in parentheses indicates the weight of the connector beam including the embedded strain gauge sensor.

While the overall dimensions of the model are precisely maintained according to the scale factor, the geometry of each floater type has been simplified for fabrication. A summary of the model components can be found in **Table 2**, and the following conditions were applied during model development:

- The geometry and orientation of PV panels are not modeled; only their weight is considered.
- The floaters are assumed to be rigid and made of Stryfoam to satisfy the mass scaling requirement. As shown in **Table 2**, the weight of each individual floater model is less than the required value. To achieve the target weight, additional weight is added through connector beams, sensor units, and weight-balancing components placed on the floater. The weight-balancing is made of colored plasticine and is covered with a thin plastic layer to make it waterproof.
- To capture the structural elasticity, the vertical pin connectors between floaters are modelled using connector beams, reffered to as Connector Beam A, B and C. To maintain the mass scale of overall model, each type of connector beams is made from different material and has a distict size, as outlined below:
  - *Connector Beam A* is made of polymer silicone rubber RTV (Room Temperature Vulcanizing)-226 with a Young's modulus of 750,000 N/m^2, a density of 1111 kg/m^3, dimensions of 3.0 cm (length) × 2.0 cm (width) × 1.3 cm (thickness) and weight 5.78 gr.
  - *Connector Beam B* is made of casted acrylic with a Young's modulus of 1,100,000 N/m^2, a density of 1180 kg/m^3, dimensions of 2.0 cm (length) × 1.0 cm (width) × 0.14 cm (thickness), and weight 0.33 gr.
  - *Connector Beam C* is also made of casted acrylic with a Young's modulus of 1,100,000 N/m^2, a density of 1180 kg/m^3, dimensions of 4.5 cm (length) × 2.8 cm (width) × 0.1 cm (thickness), and weight 1.4 gr.
- The Young's modulus value for RTV-226 and casted acrylic was obtained from laboratory tests in accordance with ASTM D412-98a and ASTM D638-22 respectively.
- Two different model configurations were used: Model A and Model B. The primary difference lies in the use of connector beams, as shown in **Figure 2a**. In Model A, the floaters are connected using Connector Beam A and B, along with a horizontal pin connector. This configuration allows for moment release at the point where horizontal pin connector is installed. Meanwhile, Model B employs Connector Beam A, B, and C to create fully fixed connections between the floaters. The

connector beams are positioned on top of the floaters, while the horizontal pin connector is installed at the mid-height of the floater, as shown in **Figure 2b**. The horizontal pin connector is 3D-printed using acrylonitrile butadiene styrene, or commercially known as ABS, and has a weight of 1.45 gr.

3.3. Mooring Line Model

In this experiment, four units of taut mooring line were used, one for each corner of the model, as illustrated in **Figure 2a**. The prototype is assumed to use a taut mooring system made of polyester, featuring a diameter of 0.056 m and an axial stiffness $(E)_p$ of 2.678 × 105 kN [27]. The taut mooring angle was fixed to 60°. The mooring line model was developed by using the following equation:

$$\left(\frac{\mathrm{EA}}{L}\right)_m = \left(\frac{\mathrm{EA}}{L}\right)_p \tag{9}$$

where A is the cross-sectional area of mooring line, and L is the length of mooring line.

The taut mooring model used fishing line with a diameter of 0.0005 m, the Young's modulus is 2.3 GPa, and the stiffness is 1.72 N/mm. As the value of $(EA)_m$ from the fishing line for mooring line model did not meet the required stiffness scale, a spring with a stiffness of 0.2 N/mm was attached in the middle of mooring line, as shown in **Figure 2c**. The equivalent stiffness of the mooring line model system is written as:

$$\frac{L_m}{k_e} = \frac{L_1}{k_1} + \frac{L_2}{k_2} + \frac{L_3}{k_3} \tag{10}$$

where L_m is the total length of mooring line model, k_e is the equivalent stiffness of mooring line, $L_{1,2,3}$ is the lengths of each section in mooring model, and $k_{1,2,3}$ is the stiffnesses for each section. The obtained stiffness of the mooring lines is still below the requirement.

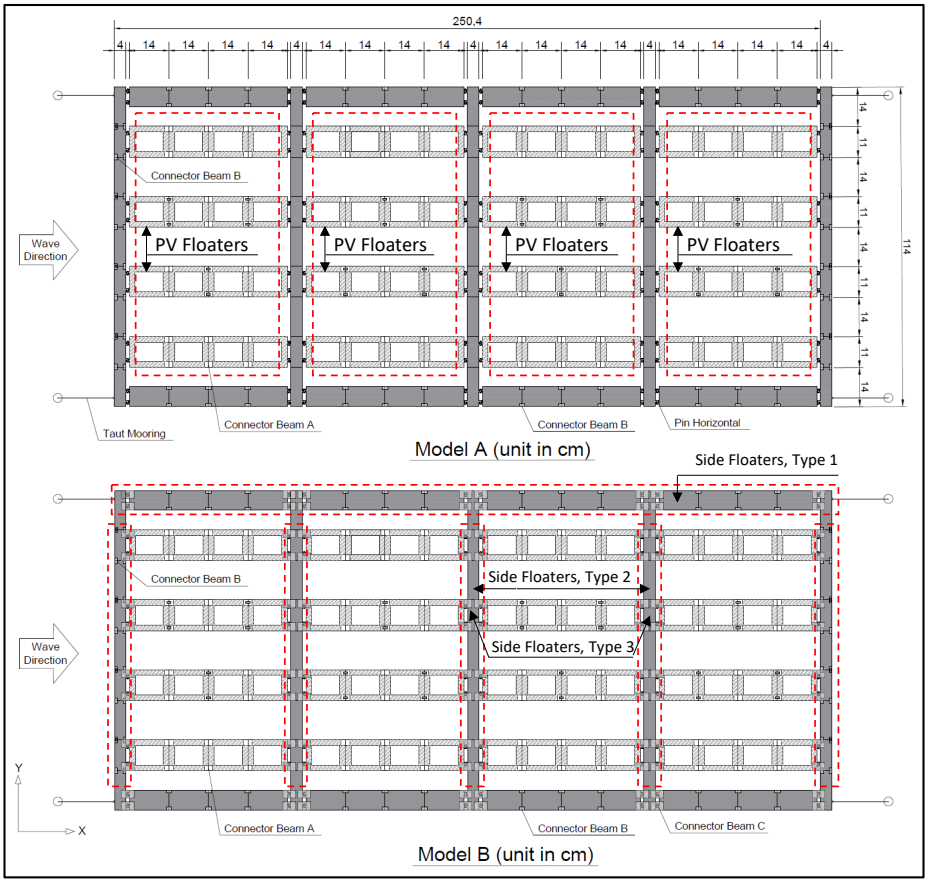

(a)

Figure 2. *Cont.*

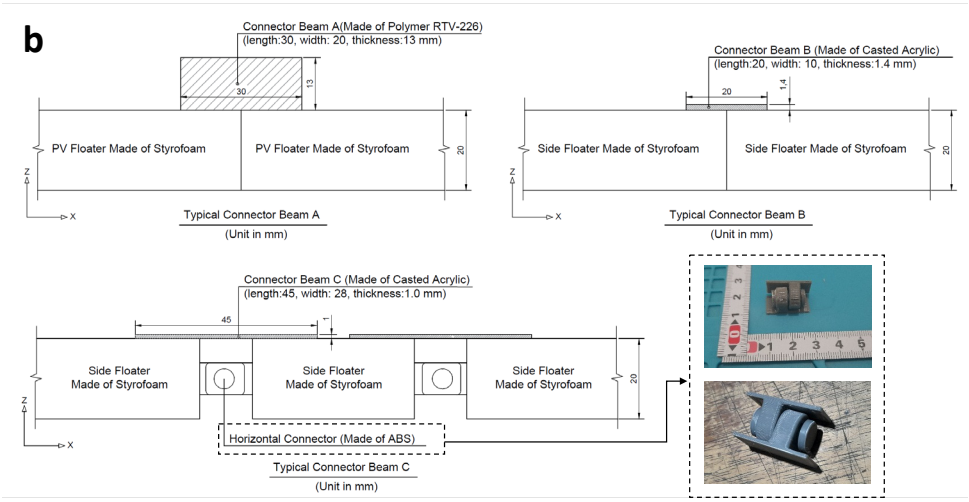

(**b**)

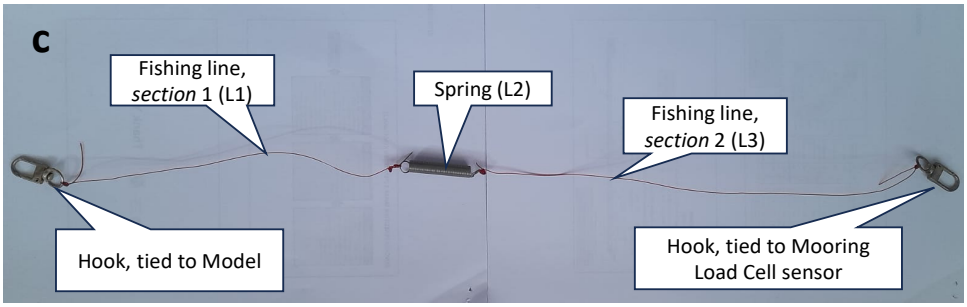

(**c**)

Figure 2. (**a**) Layout and section arrangement for Model A and B of modular FPV structure; (**b**) Typical placement of connector beams on floaters model and the horizontal pin connector; (**c**) Mooring line model.

3.4. Wave Condition

To define wave loads on the FPV structure, it is essential to consider a wave kinematic theory [10]. As illustrated in **Figure 3**, the regular waves, as defined in **Table 1,** are classified into intermediate depth categories, with wave steepness (H/L) ranging from 0.014–0.067 for a water depth of 0.6 m, and from 0.013–0.062 for a water depth of 0.8 m. By referring to the wave steepness values for intermediate depth condition, the most suitable theories for these conditions are the 3rd and 4th order Stokes theory. Wave conditions which are laid on 3rd and 5th order Cnoidal wave theory will not be analyzed in this experiment. Additionally, the JONSWAP spectrum is used for irregular waves conditions. The wave conditions pertain to the area extending from the wave generator to the area before the alteration in depth caused by the bottom profile used for examining the shoaling effect.

3.5. Modeling Scheme

The experiment involved varying the connector type, bottom profile, water depth and wave condition. The still water depth during the experiment were set at 0.8 and 0.6 m, with corresponding variations in wave height and period for each water depth, as listed in **Table 1**. Each regular wave height in **Table 1** was tested with three different wave periods, while for irregular wave heights were tested with two different peak wave periods. Two variations of bottom profile were applied: uniform bottom profile and sloping bottom profile. By applying these variations, there were 48 combinations under regular waves and 16 combinations under irregular waves applied for each Model A and B. Each combination for regular waves was run for 300 s, whereas for irregular waves were run for 1000 × T_p to capture fully developed sea conditions.

The sensors defined in Section 4 were integrated into the model, with Model A and B utilizing the same

structure. For the experimental setup involving Model B, Connector Beam C was adhered to the floater surface. This connector will be trimmed for the scheme using Model A; however, the trimming involves only 0.5 cm in the middle of the beam, resulting in a negligible additional weight (less than 0.5 grams) added to the floater unit where the connector beam was attached. This additional weight is considered insignificant for this experiment. The overall modeling scheme was organized sequentially to optimize preparation time related to the installation and removal of the bottom profile.

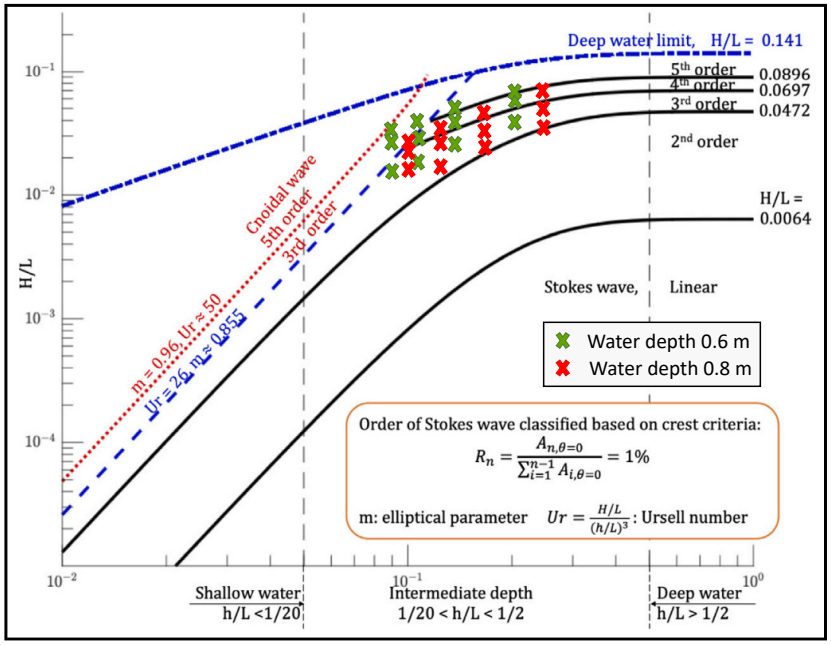

Figure 3. Wave theory for regular wave conditions (modified graph from Zhao et al., 2024 [28]).

4. Experimental Setup

4.1. Instruments Description

The experiment was undertaken in a two-dimensional wave flume located in the wave laboratory of Ocean Engineering at Bandung Institute of Technology. The wave flume measures 40 m long, 1.4 m high and 1.2 m wide, featuring glass walls and steel frames. It has passive wave dampers at both ends of the wave flume and an HR-Wallingford piston-type wave generator to generate both regular and irregular waves. The wave generator is capable to generate waves with periods ranging from 1.0 to 10.0 s, and a maximum wave height of 0.4 m at water depth of 0.8 m. The wave generator is numerically controlled, and equipped with a mechanism capable of absorbing reflected wave.

Waves were recorded by using four units of resistivity wave gauge (WG) with a sampling frequency of 100 Hz, and the data acquisition system for the WG used HR DAQ software. To validate the WG's output, the water level fluctuation at each WG was also recorded by using a mobile phone camera with a frame rate of 30 frames per second. The camera was mounted on a tripod outside the wave flume and aligned with the water level. Area-1 to 4 indicates the group of wave gauges, which were arranged to measure the same water wave surface independently and simultaneously. A digital camera also was used to record the FPV model movement in Area-5, while scale rulers were attached vertically to the wave flume wall at the position of each wave gauge to function as a benchmark for the motion tracking software in processing wave height from the video image. Model arrangements for the aforementioned conditions for water depth 0.8 m (80 cm) with uniform and sloping bottom profiles are shown in **Figure 4**. A similar arrangement applied for a water depth of 0.6 m. The height bottom profile was 0.25 m with a front slope of 1:10, made from plywood with a thickness of 1.0 cm and mounted on a steel frame.

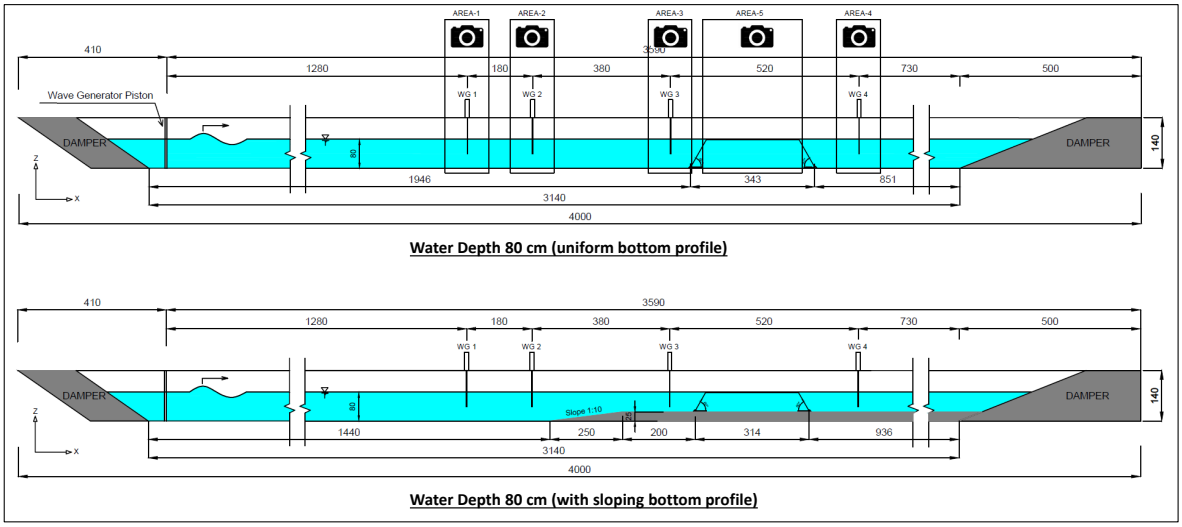

Figure 4. Wave gauges (WGs), FPV model, and digital cameras arrangement during experimental for water depth 80 cm.

4.2. Self-Developed Sensors and Data Acquisition System

In order to capture the model responses and tension under various wave loads, there were several types of sensors installed on the surface of the FPV model and connected to the model. There were 32 units of Strain Gauge (SG) to measure tension in the connection between floaters; 9 units of Inertia Motion Unit (IMU) to measure the displacement of the model in the X, Y and Z-axis; and 4 units of Mooring Load Cell (SGMO) to measure mooring line tension. The arrangement of all sensors, as shown in **Figure 5** was applied for both Model A and B. Since the IMUs and SGs were mounted on top of the model, they must be assembled as lightly as possible so that the weight of the floater-sensor-cable in the model does not surpass the total weight of the scaled floater and PV panel.

The IMUs used the DFROBOT M027-series, and the sensors were enclosed in a small box, coated with RTV-226 for waterproofing, and placed on the floater using a Velcro strap, as shown in **Figure 6a**. The total weight of the IMU, including the Velcro strap, is 5.79 grams. The IMU outputs include: gravity acceleration, magnetic earth field, acceleration, and Euler state along the X, Y and Z-axes. Pitch is represented by Euler state in the Y-axis, while heave is obtained through the double integration of acceleration value in the Z-axis. Proper positioning of the IMU is crucial for aligning its axis system with the model system.

The SGs were embedded in Connector Beams A and B, with arrangement as shown in **Figure 5**. The SG embedded in Connector Beam A used a half Wheatstone bridge load cell, with a total weight of 7.27 grams for the SG and the connector beam combined. The SG in Connector Beam B used a quarter Wheatstone bridge, as the beam size is substantially smaller than Connector Beam A. The total weight of Connector Beam B with the SG sensor is 1.25 grams. The SGMOs used a full Wheatstone bridge load cell with a capacity of 200 N. Similar to IMUs, the load cell for SGMO was also coated with RTV-226 for waterproofing. The SGMOs were developed and mounted on the bottom profile in a manner to minimizes the uplift force, as shown in **Figure 6b**. The output of SGs and SGMOs is measured in strain, expressed in gram Newton (g.N).

The SGs and SGMOs were defined into six block sensors (Block A, B, D, F, H and I); each block was connected to an ESP32 micro-controller unit (MCU), meanwhile each IMU had its own MCU. All sensors operated at a sampling frequency of 20 Hz, and the measured data from each sensor were transmitted to the data logger using Bluetooth. CoolTerm was used for interface communication with serial devices. This

software is a free and open-source serial communication application, and is commonly used for experiments involving sensors and MCUs [29,30]. This program installed in the computer, allows multiple devices to connect to a single unit computer at the same time. The schematic diagram and output for IMUs, SGs and SGMOs are shown in **Figure 6a** and **Figure 6b**. All sensors were calibrated to assess their accuracy and determine any necessary corrections. The calibration results of SGs and SGMOs demonstrated high accuracy for the given load with R^2 values exceeding 0.92. The IMUs were calibrated based on the manufacturer's guidelines by moving them both rotationally and linearly.

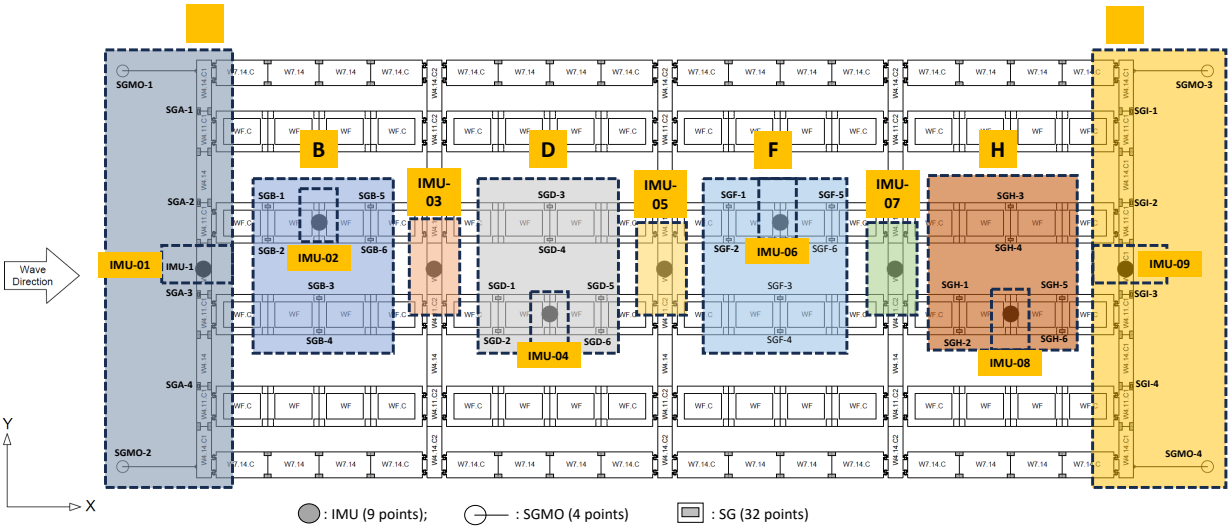

Figure 5. Sensor block diagram for IMUs, SGMOs, and SGs.

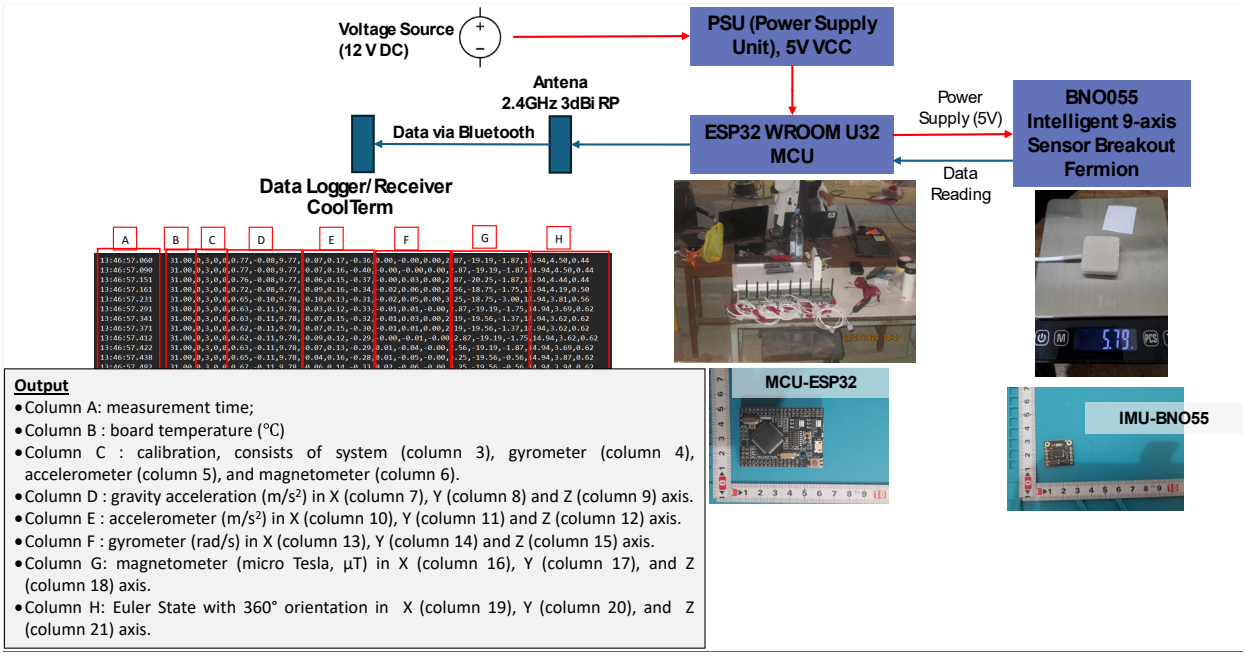

(**a**) Schematic diagram and output for IMUs.

Figure 6. *Cont.*

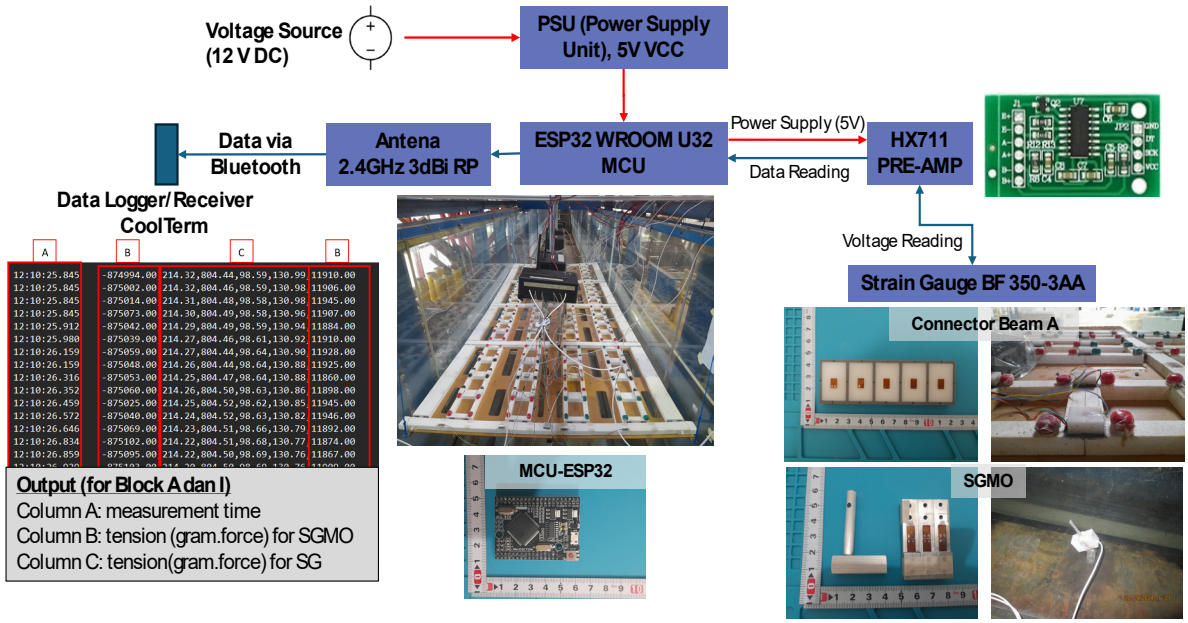

(**b**) Schematic diagram and output for SGs and SGMOs **.**

Figure 6. The schematic diagram and output for IMUs, SGs and SGMOs.

5. Results

5.1. Model Performance

The occurrence of over wash **(Figure 7a)** in the front row area was caused by surface waves over the floating array, as well as water fluctuation **(Figure 7b)** within the cavities of PV floaters, between rows of PV floaters, and between the PV floaters-side floaters row. This phenomenon is confirmed in Sree et al. (2022) [31]. Higher over wash in the front row area is attributed to the effect of taut moorings. Visual observations indicate that the motion responses of both models exhibit a propensity for higher heave response with increased wave heights. This result aligns with the finding of Shi et al. (2025) [32].

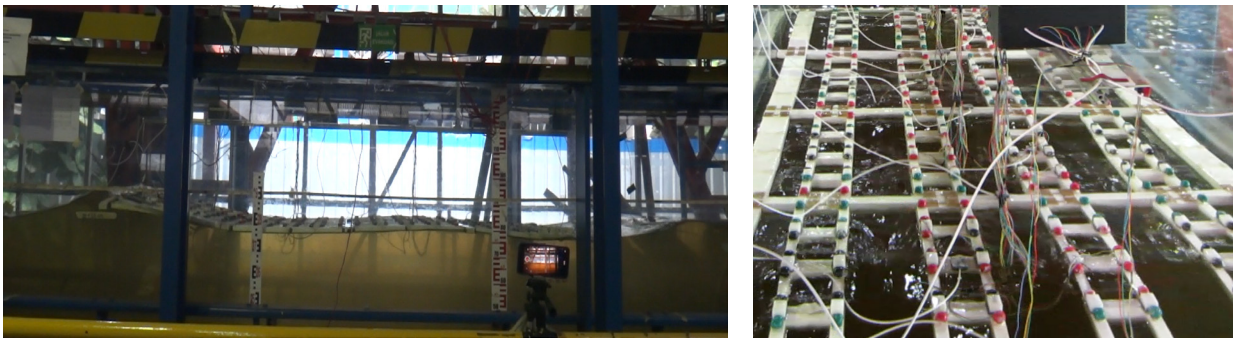

(**a**) (**b**)

Figure 7. (**a**) Over-wash over the floating array; (**b**) water fluctuation inside the cavity of floating array.

5.2. Wave Gauge Performance

Figure 8a shows the measured incident wave height at WG-1 (H_{WG-1}) in comparison to the wave height that was inputted on the wave generator software (H_{input}) for all wave period variations. The slashed solid line y

= x represents the correlation between $H_{WG\text{-}1}$ and H_{input}, as a benchmark. The measured wave heights predominantly fall below this benchmark, indicating that they are generally less than the input values. The results from WG-1 are further validated using video motion tracking (tracker). **Figure 8b** compares the wave heights from WG-1 ($H_{WG\text{-}1}$) and tracker ($H_{Tracker}$). Despite minor over-prediction of wave height by WG-1 in high wave height cases (greater than 0.15 m), the trend line of the wave height comparison follows the y = x line, suggesting that the WG-1 results are properly calibrated. Combined with the H_{input} comparison, the results show two minor issues that need to be addressed:

1. Over-prediction of wave gauge readings, especially in the large wave height range
2. The wave generator tends to generate wave heights that are lower than intended

The first issue can be mitigated by combining wave gage readings with the tracking method in large wave height cases. To address the second issue, the actual generated wave height should be used as the basis to calibrate the wave input in the wave generator software.

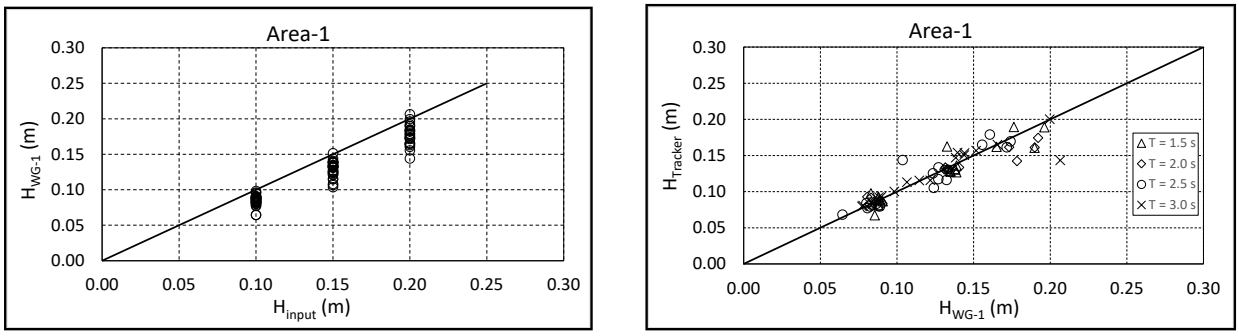

(**a**) (**b**)

Figure 8. Comparison results for wave heights; (**a**) WG-1 versus wave height input, (**b**) WG-1 versus video tracking.

5.3. Self-Developed Sensors Performance

The SGs, SGMOs, and IMUs were working properly in measuring the tension, acceleration and pitch of the structure; however, the CoolTerm software intermittently freezes while receiving data over Bluetooth. Regardless of the software-related issues, signal loss is consistently observed during data recording, with the Bluetooth signal from blocks A, B, D, F, H and I are undetectable by the receiver in the computer. This occurs despite the fact that the distance between the transmitter and receiver is merely 10 meters, significantly less than the Bluetooth antenna's specific range of 100 meters. These conditions result in data loss and reduced data quality. To ensure data quality, the corresponding modeling schemes must be repeated whenever the software freezes.

The sensor outputs for pitch (R_y) from the IMUs, as well as tension from the SGs and SGMOs can be directly used, as shown in **Figures 9a–c**. However, deriving heave from acceleration necessitates data processing. The time domain integration method is applied to derive heave (Z_h) from acceleration in the Z-axis (the heave result is shown in **Figure 9d**), but this result is lower than actual heave. **Figure 10a** and **Figure 10b** show the comparison result of the mean value of heave based on motion tracking software and time domain integration method for each IMU position (X_h) along the model (L_f) for regular wave height of 0.1 and 0.15 m with a uniform bottom profile scheme for Model B, indicating that the results from each IMU exhibit low accuracy, with the standard deviation increasing as the wave height increases. For H = 0.1 m, the standard deviation for IMUs 1-9 ranges from 0.005 to 0.32 m; meanwhile, for H = 0.15 m, the range is from 0.007 to 0.46 m.

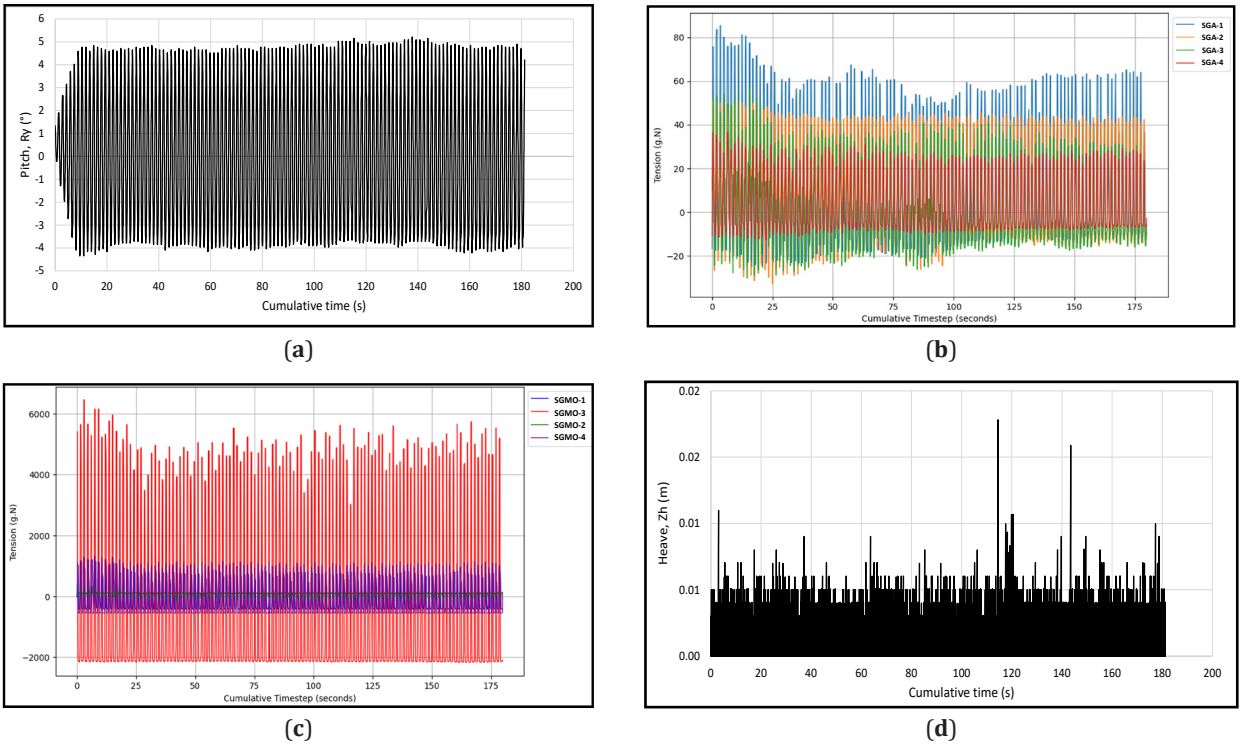

Figure 9. The sensor output for Model B with uniform bottom profile under scenario H = 0.1 m, T = 1.5 s, h = 0.6 m; (**a**) Pitch; (**b**) Tension in Connector Beams Block A; (**c**) Tension SGMOs; (**d**) Heave.

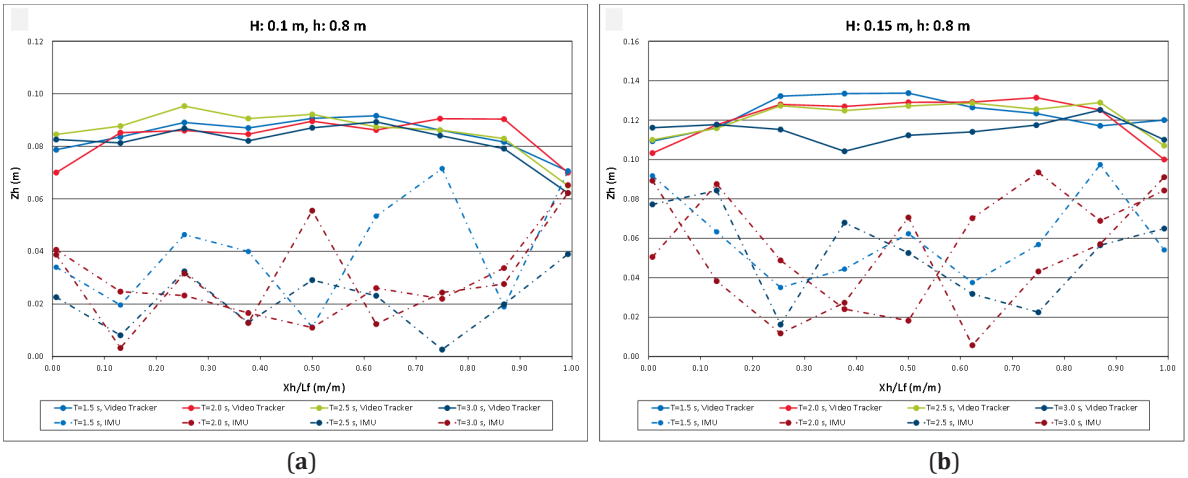

(**a**) (**b**)

Figure 10. Comparison between IMU and Video Tracker for mean heave value along the model for uniform bottom profile scheme: (**a**) H = 0.1 m, h = 0.8 m; (**b**) H = 0.15 m, h = 0.8 m.

6. Discussion

Various factors contribute to discrepancies in wave measurement, with the primary sources being the wave generator and the measurement instrument. Calibration testing for both the wave generator and wave gauges, with repeated tests, is necessary to determine the mean standard error of the estimations derived from the linear regression analysis of calibration data [33]. Due to the inconsistencies between the wave input value and the measurement result, it is necessary to define new input values by linear regression analysis based on the calibration measurements.

Wave height validation results obtained through video tracking are highly dependent on video resolution, camera perspective, and angle. An oblique angle

can distort the apparent height of waves, particularly when the camera is not positioned directly perpendicular to the wave crest-trough direction, which can lead to either overestimation or underestimation of wave height.

The mean value of heave for each IMU, derived from the time domain integration method, is significantly lower than the results obtained from the video tracker. This is mainly caused by trend-term interference or drift error on the low frequency noise, frequently occurring during the integration of acceleration to displacement [34]. The loss of data for a certain period during recording due to aforementioned reasons also affected the integration result. According to this finding, the heave obtained from this experiment later on is based on the video tracking results. The only data extracted from IMU in this experiment is pitch.

The mooring tension for SGMO-3 is significantly higher compared to SGMO-1, 2, and 4, as shown in **Figure 9c.** This difference is attributed to various factors, mainly: non-uniform length of mooring line-spring model and the asymmetry of wave front received by the floating model. The non-uniform lengths led to uneven pretensions; highlighting the importance of ensuring that all mooring lines are of equal length. An initial check under a steady condition (without wave load) is necessary to verify the uniformity of all mooring lines.

Considering the experimental setup, data acquisition system and measurement results, there are several factors that needs to be carefully adjusted for the next similar experiment. For experiments involving various types and a large number of sensors, using robust software such as NI-LabView for communicating with serial devices is advisable. However, this software can be costly, as NI-LabView is neither free nor open-source. Moreover, the utilization of 18 Bluetooth channels transmitting data at the same frequency and in close proximity results in signal interference that disrupts Bluetooth connectivity, leading to decreased performance or even total disconnection, which frequently occurs during data recording. This situation may improve by reducing the number of Bluetooth channels or by replacing the Bluetooth system with a wired data transmission system.

7. Conclusion

This paper details the scaling and modeling process for a 2-D modular FPV physical model that incorporates the hydroelasticity effect. By applying the Froude-Cauchy scaling law and utilizing composite materials, the model effectively represents wave-structure interactions under hydroelastic conditions. Calibration on the wave generator is mandatory, as the wave is the primary load in this experiment.

Details on the self-developed sensors designed and their performances to measure structural-mooring tension and structural movement in response to wave loads are also presented. While the sensors are functioning properly, there is a need for enhancements in the data acquisition system to improve the quality of the recorded data. Additionally, video recording methods used to validate wave height and heave have yielded promising results.

While the equivalent stiffness of the mooring lines in this experiment does not fully satisfy Froude scaling requirements, the configuration was designed to maintain functional similarity in terms of restoring behaviour and boundary constraints. In practice, exact dynamic scaling of mooring stiffness in small-scale experiments is extremely challenging due to material limitations and nonlinearities in mooring system behaviour. For a similar 2-D experiment, the use of soft mooring or the exclusion of the mooring system is considered.

Statistical analysis based on repeated experimental runs is essential in this type of experiment to ensure the reliability, repeatability, and robustness of the results. Due to the complex, dynamic interactions between waves, FPV model, and mooring systems, individual test runs may be influenced by uncontrolled variables such as slight differences in wave generation, sensor noise, or environmental disturbances in the laboratory setting. In this experiment, while the findings are based on single-run measurements, the observed trends in heave and pitch along the model show agreement with the references.

Author Contributions

Conceptualization, Methodology, Resources, Investigation, Formal Analysis, Visualization, Writing-Original Draft Preparation, Funding Acquisition, Administration, M.A.N.; Supervision, Writing-Review & Editing, R.L.T.; Conceptualization, Methodology, Supervision, Writing-Review & Editing, A.M.F., E.C.I., and F.P.B.; Investigation, Visualization, Software, A.S.M., M.R.K., and R.A.Z.; Resources, Investigation, A.A., A.P.K.H., H.F., J.A., and N.L.S. All authors have read and agreed to the published version of the manuscript.

Funding

This research is funded by the Center for Higher Education Funding and Assessment (Pusat Pelayanan Pembiayaan dan Asesmen Pendidkan Tinggi)-Ministry of Higher Education, Science, and Technology of Republic Indonesia.

Institutional Review Board Statement

Not applicable.

Informed Consent Statement

Not applicable.

Data Availability Statement

Data is available upon request to the corresponding author.

Acknowledgments

Acknowledgment for Flot Indonesia for technical data support of the modular FPV structure, and OC-Enviro for model, sensors and data acquisition system development.

Conflicts of Interest

The authors declare no conflict of interest.

References

[1] Fan, S., Ma, Z., Liu, T., et al., 2025. Innovations and development trends in offshore floating photovoltaic systems: A comprehensive review. Energy Reports. 13, 1950–1958. DOI: https://doi.org/10.1016/j.egyr.2025.01.053

[2] Liu, G., Guo, J., Peng, H., et al., 2024. Review of Recent Offshore Floating Photovoltaic Systems. Journal of Marine Science and Engineering. 12(11), 1942. DOI: https://doi.org/10.3390/jmse12111942

[3] Claus, R., López, M., 2022. Key issues in the design of floating photovoltaic structures for the marine environment. Renewable and Sustainable Energy Reviews. 164, 112502. DOI: https://doi.org/10.1016/j.rser.2022.112502

[4] Naiborhu, M.A., Firdaus, A.M., Bakti, F.P., et al., 2025. Scaling and modeling strategy for two-dimensional physical model of near-shore floating photovoltaic structure. IOP Conference Series: Earth and Environmental Science. 1464(1), 012024. DOI: https://doi.org/10.1088/1755-1315/1464/1/012024

[5] Shi, W., Yan, C., Ren, Z., et al., 2023. Review on the development of marine floating photovoltaic systems. Ocean Engineering. 286, 115560. DOI: https://doi.org/10.1016/j.oceaneng.2023.115560

[6] Zhang, C., Dai, J., Ang, K.K., et al., 2024. Development of compliant modular floating photovoltaic farm for coastal conditions. Renewable and Sustainable Energy Reviews. 190, 114084. DOI: https://doi.org/10.1016/j.rser.2023.114084

[7] EDP Renewables, 2024. Floating Solar. Available from: https://www.edpr.com/apac/en/Renewable-solutions/utility-scale/floating-solar (cited 15 August 2025).

[8] Choi, D.-H., Jeon, J.-M., Maeng, M.-J., et al., 2024. Experimental and numerical study on motion responses of modular floating structures with connectors in waves. Ocean Systems Engineering. 14(3), 277–299. DOI: https://doi.org/10.12989/OSE.2024.14.3.277

[9] Jiang, D., Tan, K.H., Wang, C.M., et al., 2021. Research and development in connector systems for Very Large Floating Structures. Ocean Engineering. 232, 109150. DOI: https://doi.org/10.1016/j.oceaneng.2021.109150

[10] Fu, S., Moan, T., Chen, X., et al., 2007. Hydroelastic analysis of flexible floating interconnected

structures. Ocean Engineering. 34(11–12), 1516–1531. DOI: https://doi.org/10.1016/j.oceaneng.2007.01.003

[11] Kim, B.W., Hong, S.Y., Lee, K., 2025. Time Domain Stress and Fatigue Life Evaluation for the Connector of a Floating Multi-Body in Waves by Total Beam and Local Shell Analyses. Journal of Ocean Engineering and Technology. 39(3), 264–275. DOI: https://doi.org/10.26748/KSOE.2025.001

[12] Liu, X., Sakai, S., 2002. Time Domain Analysis on the Dynamic Response of a Flexible Floating Structure to Waves. Journal of Engineering Mechanics. 128(1), 48–56. DOI: https://doi.org/10.1061/(ASCE)0733-9399(2002)128:1(48)

[13] Li, Z., Chen, D., Feng, X., 2023. Hydroelastic and expansibility analysis of a modular floating photovoltaic system with multi-directional hinge connections. Ocean Engineering. 289, 116218. DOI: https://doi.org/10.1016/j.oceaneng.2023.116218

[14] Jiang, C., El Moctar, O., Zhang, G., 2024. Nonlinear modeling of wave-structure interaction for a flexible floating structure. Ocean Engineering. 300, 117489. DOI: https://doi.org/10.1016/j.oceaneng.2024.117489

[15] Shi, Y., Wei, Y., Tay, Z.Y., et al., 2023. Hydroelastic analysis of offshore floating photovoltaic based on frequency-domain model. Ocean Engineering. 289, 116213. DOI: https://doi.org/10.1016/j.oceaneng.2023.116213

[16] Xu, P., Wellens, P.R., 2022. Fully nonlinear hydroelastic modeling and analytic solution of large-scale floating photovoltaics in waves. Journal of Fluids and Structures. 109, 103446. DOI: https://doi.org/10.1016/j.jfluidstructs.2021.103446

[17] Zhang, M., Schreier, S., 2022. Review of wave interaction with continuous flexible floating structures. Ocean Engineering. 264, 112404. DOI: https://doi.org/10.1016/j.oceaneng.2022.112404

[18] Chakrabarti, S., 1998. Physical Model Testing of Floating Offshore Structures. Offshore Structure Analysis, Inc: Plainfield, IL , USA. Available from: https://dynamic-positioning.com/proceedings/dp1998/DSubrata.PDF

[19] Ruzzo, C., Muggiasca, S., Malara, G., et al., 2021. Scaling strategies for multi-purpose floating structures physical modeling: state of art and new perspectives. Applied Ocean Research. 108, 102487. DOI: https://doi.org/10.1016/j.apor.2020.102487

[20] Vassalos, D., 1998. Physical modelling and similitude of marine structures. Ocean Engineering. 26(2), 111–123. DOI: https://doi.org/10.1016/S0029-8018(97)10004-X

[21] Bakti, F.P., Jin, C., Kim, M.-H., 2021. Practical approach of linear hydro-elasticity effect on vessel with forward speed in the frequency domain. Journal of Fluids and Structures. 101, 103204. DOI: https://doi.org/10.1016/j.jfluidstructs.2020.103204

[22] Jin, C., Lee, I., Bakti, F., et al., 2025. Multi-body-based 2D hydro-elasticity simulations in time domain for moored floating structure. Engineering Structures. 329, 119789. DOI: https://doi.org/10.1016/j.engstruct.2025.119789

[23] Loe, P.Y.A., Kim, M., Jin, C., et al., 2025. Recent advances in Discrete-Module-Beam-based hydroelasticity method as an efficient tool approach for continuous very large floating structures. Ocean Engineering. 340, 122229. DOI: https://doi.org/10.1016/j.oceaneng.2025.122229

[24] Rajendran, S., Guedes Soares, C., 2016. Numerical investigation of the vertical response of a containership in large amplitude waves. Ocean Engineering. 123, 440–451. DOI: https://doi.org/10.1016/j.oceaneng.2016.06.039

[25] Hughes, S.A., 1993. Physical Models and Laboratory Techniques in Coastal Engineering, Advanced Series on Ocean Engineering. WORLD SCIENTIFIC: London, UK. p.25. DOI: https://doi.org/10.1142/2154

[26] Dai, J., Zhang, C., Lim, H.V., et al., 2020. Design and construction of floating modular photovoltaic system for water reservoirs. Energy. 191, 116549. DOI: https://doi.org/10.1016/j.energy.2019.116549

[27] Luo, W., Zhang, X., Tian, X., et al., 2024. Conceptual design and model test of a pontoon-truss type offshore floating photovoltaic system with soft connection. Ocean Engineering. 309, 118518. DOI: https://doi.org/10.1016/j.oceaneng.2024.118518

[28] Zhao, K., Wang, Y., Liu, P.L.-F., 2024. A guide for selecting periodic water wave theories - Le Méhauté (1976)'s graph revisited. Coastal Engineering. 188, 104432. DOI: https://doi.org/10.1016/j.coastaleng.2023.104432

[29] Abdullahi, S.I., Habaebi, M.H., Gunawan, T.S., et al., 2017. Miniaturized Water Flow and Level Monitoring System for Flood Disaster Early Warning. IOP Conference Series: Materials Science and Engineering. 260, 012019. DOI: https://doi.

org/10.1088/1757-899X/260/1/012019

[30] Daud, S.A., Mohd Sobani, S.S., Ramiee, M.H., et al., 2013. Application of Infrared sensor for shape detection. In Proceedings of the 2013 IEEE 4th International Conference on Photonics (ICP). Melaka, Malaysia, 28–30 October 2013; pp. 145–147. DOI: https://doi.org/10.1109/ICP.2013.6687095

[31] Sree, D.K.K., Law, A.W.-K., Pang, D.S.C., et al., 2022. Fluid-structural analysis of modular floating solar farms under wave motion. Solar Energy. 233, 161–181. DOI: https://doi.org/10.1016/j.solener.2022.01.017

[32] Shi, Y., Wei, Y., Chen, K., et al., 2025. Frequency-domain approach of hydroelastic response for flexible offshore floating photovoltaic under combined wind and wave loads. Ocean Engineering. 323, 120565. DOI: https://doi.org/10.1016/j.oceaneng.2025.120565

[33] Sener, M.Z., Yoon, H.K., Nguyen, T.T.D., et al., 2023. An experimental study on capacitive and ultrasonic measurement principles and uncertainty assessment in laboratory wave measurements. Ocean Engineering. 285, 115320. DOI: https://doi.org/10.1016/j.oceaneng.2023.115320

[34] Zhu, H., Zhou, Y., Hu, Y., 2020. Displacement reconstruction from measured accelerations and accuracy control of integration based on a low-frequency attenuation algorithm. Soil Dynamics and Earthquake Engineering. 133, 106122. DOI: https://doi.org/10.1016/j.soildyn.2020.106122